Surface Water and Ocean Topography Project

Level 2 Radiometer Algorithm Theoretical Basis Document

Initial Release

Prepared by:

Electronic signature on file	07/24/2023
Chun Sik Chae JPL AMR Algorithm Engineer	Date

Approved by:

Electronic signature on file	07/31/2023	Email approval on file	8-1-2023
Curtis Chen JPL Algorithm System Engineer	Date	Nicolas Picot CNES Algorithm System Engineer	Date

Concurred by:

Email approval on file	7/25/2023	Email approval on file	8-1-2023
Lee Fu JPL Project Scientist	Date	Rosemary Morrow CNES Oceans Science Lead	Date

Paper copies of this document may not be current and should not be relied on for official purposes. The current version is in the JPL Product Data Management System (EPDM: https://epdm.jpl.nasa.gov) and the CNES Product Data Management System

July 16, 2023
JPL D-105809

National Aeronautics and Space Administration
Jet Propulsion Laboratory
California Institute of Technology

Contributing Authors

Name	Affiliation
Tanvir Islam	Jet Propulsion Laboratory, California Institute of Technology
Shailen Desai	Jet Propulsion Laboratory, California Institute of Technology

Science Team Reviewers

Name	Affiliation
Shannon Brown	Jet Propulsion Laboratory, California Institute of Technology
Bruno Picard	Fluctus SAS

Electronic Signatures in EPDM

User-Group/Role	...	Decision	Comments	Date
Murillo, Sylvia (murillo)-CM and IM/CME	...	Approve	Signing for Lee-Lueng Fu	25-Jul-2023 12:12
Chen, Curtis W (curtis)-JPL Consumer/Project Consumer	...	Approve		31-Jul-2023 08:16
Chae, Chun Sik (cchae)-JPL Author/JPL Author WIP	...	Approve		24-Jul-2023 14:18

Change Log

VERSION	DATE	SECTIONS CHANGED	REASON FOR CHANGE
Initial Release	2020-07-16	ALL	Initial Release Approved for public release (URS317788/CL#23-3545)

Table of Contents

Table of Figures

Table of Tables

List of TBC Items

These items are to be completed when document is ready to enter configuration control.

Page	Section

List of TBD Items

These items are to be completed when document is ready to enter configuration control.

Page	Section

1 Introduction

1.1 Purpose

The purpose of this Algorithm Theoretical Basis Document (ATBD) is to describe the physical and mathematical basis for the science data processing algorithms that are used to generate the SWOT Level 2 Advanced Microwave Radiometer (AMR) Geophysical Data Record (GDR) science data product (L2_RAD_GDR). These algorithms are independent of latency and are therefore also used to create the shorter latency Operational GDR (OGDR) and Interim GDR (IGDR) versions of the radiometer product. The short latency OGDR and IGDR versions of the product use best available dynamic calibration coefficients and orbit ephemeris products, while the GDR requires availability of calibration coefficients for the repeat cycle being processed as well as the precise orbit ephemeris.

1.2 Scope

The scope of this document is to:

1. Identify the list of primary functions that compose the Level 2 processing steps and their flow. These functions are broken down by the primary functional steps involved in the processing.
2. Describe the purpose of each of the functions.
3. Describe the input data to each function.
4. Describe the output data from each function.
5. Describe the mathematical basis of the algorithm in each function.
6. Describe the expected accuracy and/or limitations of the algorithm in each function.
7. Provide the relevant references for the algorithms described in this document.

1.3 Document Organization

Section 1 provides the purpose and scope, of this document.

Section 2 provides the background and context of the algorithms described in this document, and the functional flow of the primary functions (e.g., block diagram).

Section 3 provides the algorithm description for each of the functions shown in the block diagram, including input data, output data, mathematical basis, and expected accuracy.

Section 4 provides references for the algorithms described in this document.

Appendix A provides a listing of the acronyms used in this document.

2 Overview

2.1 Background and Context

The Surface Water and Ocean Topography (SWOT) mission is a partnership between two communities, physical oceanography and hydrology, to share high vertical accuracy topography data produced by the payload, whose principal instrument is the Ka-band Radar Interferometer (KaRIn). The details of SWOT mission objectives and requirements can be found in the SWOT Science Requirements Document [1]. The broad scientific goals can be summarized as follows:

Oceanography: characterize the ocean mesoscale and submesoscale circulation determined from the ocean surface topography at spatial resolutions of 15 km (for 68% of the ocean).

Hydrology: To provide a global inventory of all terrestrial surface water bodies whose surface area exceeds $(250\text{m})^2$ (goal: $(100\text{m})^2$, threshold: 1km^2) (lakes, reservoirs, wetlands) and rivers whose width exceeds 100m (goal: 50m, threshold: 170m). To measure the global storage change in terrestrial surface water bodies at sub-monthly, seasonal, and annual time scales. To estimate the global change in river discharge at sub-monthly, seasonal, and annual time scales.

This document describes the Level 2 processing steps that are used to generate the L2_RAD_GDR science data product [2]. The purpose of L2_RAD_GDR product is to provide measurements of wet troposphere content measured by the radiometers onboard SWOT. There are two simultaneously active radiometers onboard SWOT. The two SWOT radiometers are named the "+y" and "–y" strings and operate independently from each other. Each radiometer has a single feed that illuminates the 1-meter primary reflector to produce two beams on the ground. The names of the two strings are a reference to the location (+y or -y) of the two beams relative to the y-axis of the spacecraft body-fixed frame. The two radiometers facilitate measurements on the left and right sides of the satellite nadir point, approximately half-way across each of the two KaRIn swaths (See Figures 1 and 2 from [2]). The beam of one radiometer is aligned approximately 4.5 degrees (~70 km) fore and the other is 4.5 degrees (~70 km) aft of the satellite nadir point. Each of the radiometers operate at three frequencies, 18.7, 23.8, and 34.0 GHz. The algorithms described here are applied independently to the measurements from each side to generate the independent measurements provided on the L2_RAD_GDR product [2]. The radiometer measurements of wet troposphere content are only applicable over oceans, and therefore only applicable to over-ocean measurements from the nadir altimeter and KaRIn. The KaRIn hydrology processing uses meteorological models to determine the wet troposphere delays. A description of the L2_RAD_GDR science data product is provided in [2].

2.2 Functional Flow

Table 1 provides a high-level description of each of the Level 2 processing functions that are used to generate the L2_RAD_GDR product. Figure 1 then illustrates the flow of these Level 2 processing steps.

The Level 2 processing begins with the radiometer Level 1B parameters, which include main beam and equalized brightness temperatures for 3 channels (18.7, 23.8, and 34.0 GHz) and associated quality flags. These Level 1B parameters are used to compute the radiometer surface type, radiometer sea ice and rain flags, as well as the radiometer geophysical parameters, which include wet path delay, integrated cloud liquid water, integrated water vapor content, sea surface wind speed, and atmospheric attenuation of the Ku, C, and Ka band backscatter coefficients for the open ocean. A coastal algorithm is applied to compute the wet path delay near land [3]. These radiometer Level 2 parameters can then be interpolated (in time and space) to the respective locations of the nadir altimeter and KaRIn measurements.

The SWOT radiometer has two operating sides, with H and V polarization, respectively. The telemetry from each side are identified by a unique application identifier (APID). The algorithms described here are applied independently to measurements from each of the two operating sides, using calibration coefficients that are specific to each APID. The Level 2 functions that are described here are applied sequentially to each individual measurement from each operating side. More specifically, none of the functions in the Level 2 processing steps require more than one radiometer measurement.

Table 1. High level description of the functions used to generate the L2_RAD_GDR product.

Function Name	Description
RadLandFractionDistance	Computes the antenna gain weighted land fraction at the radiometer measurement location using a surface map.
RadLandSeaMask	Computes the surface type flag using antenna gain weighted land fractions at the radiometer measurement location.
RadSeaIceMask	Computes the sea ice flag at the radiometer measurement location using the equalized brightness temperatures.
RadCloudLiquidWater	Computes integrated cloud liquid water content from the equalized brightness temperatures.
RadRainMask	Computes the rain flag from equalized brightness temperatures.
RadWindSpeed	Computes sea surface wind speed from the equalized brightness temperatures.
RadPathDelaySea	Computes path delay over open oceans from equalized brightness temperatures.
RadPathDelayLand	Computes path delay over ocean but near land using main beam brightness temperatures.
RadPathDelayGlobal	Computes global over ocean path delay using the open ocean and near land estimates.
RadWaterVapor	Computes integrated water vapor content from the path delay due to vapor.
RadAttSig0	Computes atmospheric attenuation to backscatter coefficient, sigma0, at the nadir altimeter and KaRIn frequencies.

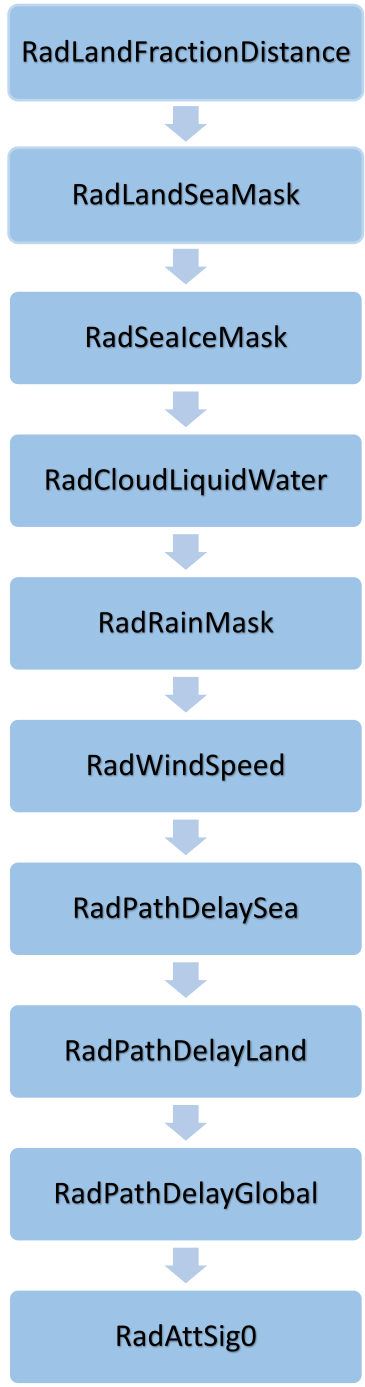

Figure 1. Flow diagram of the Level 2 processing steps (functions) used to generate the L2_RAD_GDR product.

3 Algorithm Descriptions

3.1 RadLandFractionDistance

3.1.1 Purpose

This function determines the antenna gain weighted land fraction at the radiometer measurements location from a surface map. This function also determines the radial distance to the nearest land from the radiometer measurements location from the surface map.

3.1.2 Input Data

Description	Source
Discretized map of antenna gain-weighted land fractions for each of three radiometer frequencies, with attributes for maps (number of AMR channels; number latitude and longitude bins; latitude and longitude for first node; steps in latitude and longitude).	Static Auxiliary Data
Discretized map of distance to land with attributes for map (number latitude and longitude bins; latitude and longitude for first node; steps in latitude and longitude).	Static Auxiliary Data
Latitude of AMR measurement	RadGeolocation (L1A)
Longitude of AMR measurement	RadGeolocation (L1A)

3.1.3 Output Data

Description
Antenna gain weighted land fraction in main beam of each AMR channel at the provided measurement location.
Radial distance to land at the provided measurement location.

3.1.4 Mathematical Statement

This algorithm outputs the radial distance to land of the AMR measurement and the antenna gain weighted land fraction in the AMR main beam. The frequency dependent AMR land fractions will be used in subsequent processing to correct the AMR path delay measurements near land.

The contribution of land to the AMR brightness temperature measurement is a function of the fraction of land in the AMR field of view weighted by the antenna gain in the direction of the land. Using a land mask and the AMR antenna patterns, this antenna gain weighted land fraction in the main beam can be computed for any latitude and longitude on the globe. When the sub-satellite point has Earth coordinates Lat_0, Lon_0, then the fraction of land in the AMR main beam weighted by the AMR antenna pattern is computed as:

$$LF_{MB}(Lat_0, Lon_0, f, p) = \frac{\int_0^{2\pi} \int_0^{\theta_{MB}} LandMask(\theta, \phi, Lat_0, Lon_0) P_{fp}(\theta, \phi) \sin(\theta)\, d\theta d\phi}{\int_0^{2\pi} \int_0^{\theta_{MB}} P_{fp}(\theta, \phi) \sin(\theta)\, d\theta d\phi}$$

(3.1.1)

where (θ, ϕ) are the elevation and azimuth angles from the AMR boresight, $P_{fp}(\theta, \phi)$ is the AMR spherical antenna pattern measured pre-launch for each of the three AMR frequencies (f) and two polarizations *(p)* (note: the AMR has two operating sides which have different polarizations, H and V) and $LandMask(\theta, \phi, Lat_o, Lon_0)$ is 0 if there is ocean in the direction (θ, ϕ) from the antenna boresight when centered over (Lat_o, Lon_0) and 1 if there is land in the direction (θ, ϕ) from the antenna boresight when centered over (Lat_o, Lon_0). A high resolution (2 minute by 2 minute or better) land mask is generated pre-launch using the measured antenna patterns and a reference land/ocean mask, and then used to compute the land fraction in the main beam. LF_{MB} will have a value of 0 if there is no land within θ_{MB} of boresight and will have a value of 1 if there is no ocean within θ_{MB} of boresight. The LF_{MB} value will always be between 0 and 1. The boundary of the main beam, θ_{MB} is taken to be 3^0 and is defined as the angle from beam center corresponding to horizontal separation distances at which the autocorrelation of brightness temperature is below roughly 50%, as determined from statistical analysis of a large ensemble of AMR flight data. The values of land fraction at the location of each AMR measurement are determined by bilinear interpolation in latitude and longitude of the high resolution land mask.

The distance to land is also provided using the high resolution land mask. This algorithm also performs bilinear interpolation to assign a distance to land to the measurement.

3.1.5 Accuracy

The accuracy of the land fraction estimates is a function of the accuracy of the land mask used in the generation of the discretized map and the pre-launch measurements of the spherical antenna pattern of the AMR reflector. There is some uncertainty in the land fraction estimate due to azimuthal variations in the beam patterns.

3.2 RadLandSeaMask

3.2.1 Purpose

This function determines the land/sea flag from antenna gain weighted land fraction at the radiometer measurements location.

3.2.2 Input Data

Description	Source
Land fraction threshold for land/near-land flagging	Static Auxiliary Data
Antenna gain weighted land fraction of the 18.7 GHz channel.	RadLandFractionDistance (L2)

3.2.3 Output Data

Description
Land sea mask flag at the radiometer measurement location.

3.2.4 Mathematical Statement

Because the AMR path delays are not valid when the measurements are contaminated by land, the surface type of the radiometer is needed to flag the AMR measurements. The AMR surface type is set to open ocean (0), near land (1), and land (2) using a land fraction threshold. This flag is used to determine if open ocean or near-land retrieval algorithms should be used for computation of wet troposphere delay. The land fraction threshold is based upon the following:

$$Land\ Flag = \begin{cases} 0;\ \ if\ 18.7\ GHz\ land\ fraction = 0 \\ 1;\ if\ 18.7\ GHz\ land\ fraction > 0\ and < threshold \\ 2;\ if\ 18.7\ GHz\ land\ fraction \geq threshold \end{cases} \tag{3.2.1}$$

The recommended value of the land fraction threshold is 0.5 globally, namely assuming the antenna pattern has 50% land cover regardless of any spatially dependent variation in land brightness.

3.2.5 Accuracy

The accuracy of the flag is dependent on the input surface mask and there is no associated requirement.

3.3 RadSeaIceMask

3.3.1 Purpose

This function determines the sea ice mask at the radiometer measurement's location from the radiometer brightness temperatures.

3.3.2 Input Data

Description	Source
Maximum latitude extent for sea ice	Static Auxiliary Data
Threshold on 34.0 GHz – 18.7 GHz brightness temperature difference for sea ice.	Static Auxiliary Data
Equalized brightness temperatures at each AMR channel (18.7. 23.8, and 34.0 GHz).	RadEqualizeTb (L1B)
Land/sea mask flag	RadLandSeaMask (L2)
Latitude of AMR measurement	RadGeolocation (L1A)

3.3.3 Output Data

Description
Sea ice flag

3.3.4 Mathematical Statement

Sea ice has an emissivity near 1 in the microwave and has a small frequency dependence. This contrasts from the open ocean brightness temperature. Sea ice can be identified by observing the difference between the AMR 34.0 GHz and 18.7 GHz brightness temperatures. This difference is near 20-30 K in the open ocean. It is generally less than 10K when sea ice is present. This difference is also small for land, but that can be assessed using the land flag.

The sea ice masking flag is computed using the following conditional expression:

$$f(TB_{34-18}, lat, lsm) = \begin{cases} 1; if\ TB_{34-18} < \ thres_{TB}, |lat| > \ thres_{lat}, lsm = 0 \\ 0; otherwise \end{cases} \quad (3.3.1)$$

where, TB_{34-18} is the equalized brightness temperature difference between the 34.0 GHz and 18.7 GHz channels, lat is the corresponding latitude of the measurements, lsm is the land sea masking flag information, and $thres_{TB}$ and $thres_{lat}$ are the associated thresholds in brightness temperature difference and latitude, respectively.

The recommended value for $thres_{lat}$ is 47 degrees and the recommended value for $thres_{TB}$ is 10 K. It should be noted that the AMR sea ice flag will never be set within about 25 km from land and for absolute latitudes less than $thres_{lat}$.

3.3.5 Accuracy

This algorithm is shown to give reasonable distributions for sea ice. Figure 2 shows a 100-

day average from during the southern hemisphere winter for the AMR sea ice flag. The sea ice flag will never be set for absolute latitudes less than $thres_{lat}$, over land, and over coastal oceans. A comparison of Jason-3 sea ice values with OSISAF sea edge data (i.e., OSISAF 402 Global Sea Ice Edge) shows that the algorithm has an accuracy of 96.5%. If true resolution brightness temperatures are used instead of equalized values, the error is larger due to the larger beam at 18.7 GHz.

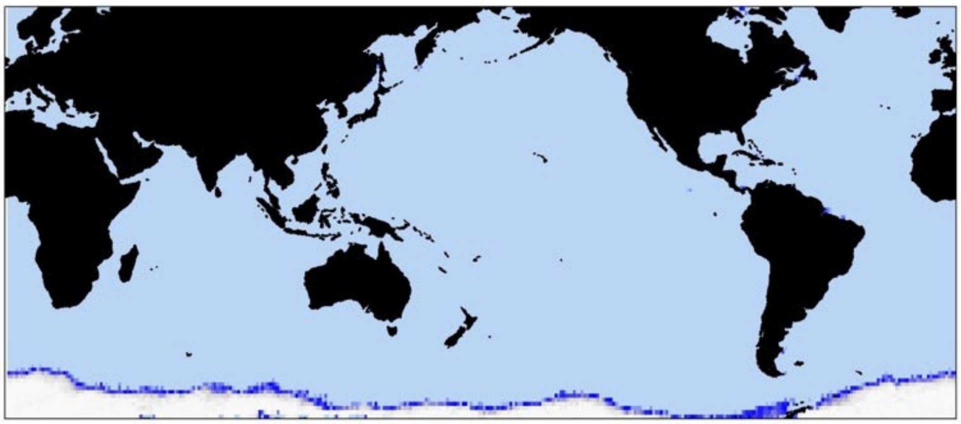

Figure 2. 100-day average of AMR sea ice flag during southern hemisphere winter. Colors represent percent of time in 100 days when sea ice flag is set. Dark blue represents where sea ice flag is set for > 0% and < 100 % of 100 days, light blue represents 0%, and white represents 100%.

3.4 RadCloudLiqWater

3.4.1 Purpose

This function computes cloud liquid water content (integrated) from the radiometer brightness temperatures.

3.4.2 Input Data

Description	Source
Retrieval coefficients to compute the integrated cloud liquid burden	Static Auxiliary Data
Equalized brightness temperatures at each AMR channel (18.7. 23.8, and 34.0 GHz).	RadEqualizeTb (L1B)
Land/sea mask flag	RadLandSeaMask (L2)
Sea ice flag	RadSeaIceMask (L2)

3.4.3 Output Data

Description
Integrated cloud liquid burden content (cloud burden)
Quality flag for cloud liquid burden

3.4.4 Mathematical Statement

This algorithm is based upon [4]. The integrated cloud liquid water content, L_z, is determined as follows:

$$L_z = L_0 + \sum_{i=1}^{3}[L(f_i) * T_b(f_i) + L_{sq}(f_i) * [T_b(f_i)]^2 + L_{cu}(f_i) * [T_b(f_i)]^3] \qquad (3.4.1)$$

where $T_b(f_i)$ are the equalized AMR brightness temperatures for each frequency, f_i, with i = 1 to 3 corresponding to the 18.7 GHz, 23.8 GHz, and 34.0 GHz frequencies, respectively. $L_0, L(f_i), L_{sq}(f_i), L_{cu}(f_i)$ are the cloud liquid retrieval coefficients.

These coefficients are derived from a regression of modeled brightness temperatures at AMR frequencies to integrated cloud liquid water. The modeled brightness temperatures are computed using atmospheric profiles from island radiosonde observations and cloud liquid water profiles from a cloud model, combined with statistical distributions of surface wind speed and sea surface temperature.

The quality flag is set to bad when the provided sea ice flag is set, and/or when the provided land/sea flag indicates land or coastal oceans.

3.4.5 Accuracy

Comparison of cloud liquid water from radiosondes and the cloud liquid water content from the algorithm using the brightness temperatures is shown in the scatter plot below. The cloud liquid water that is compared to the algorithm is derived from the radiosonde temperature and humidity profile. The accuracy of the cloud liquid water content from the radiometer brightness temperatures is 0.07 kg/m^2.

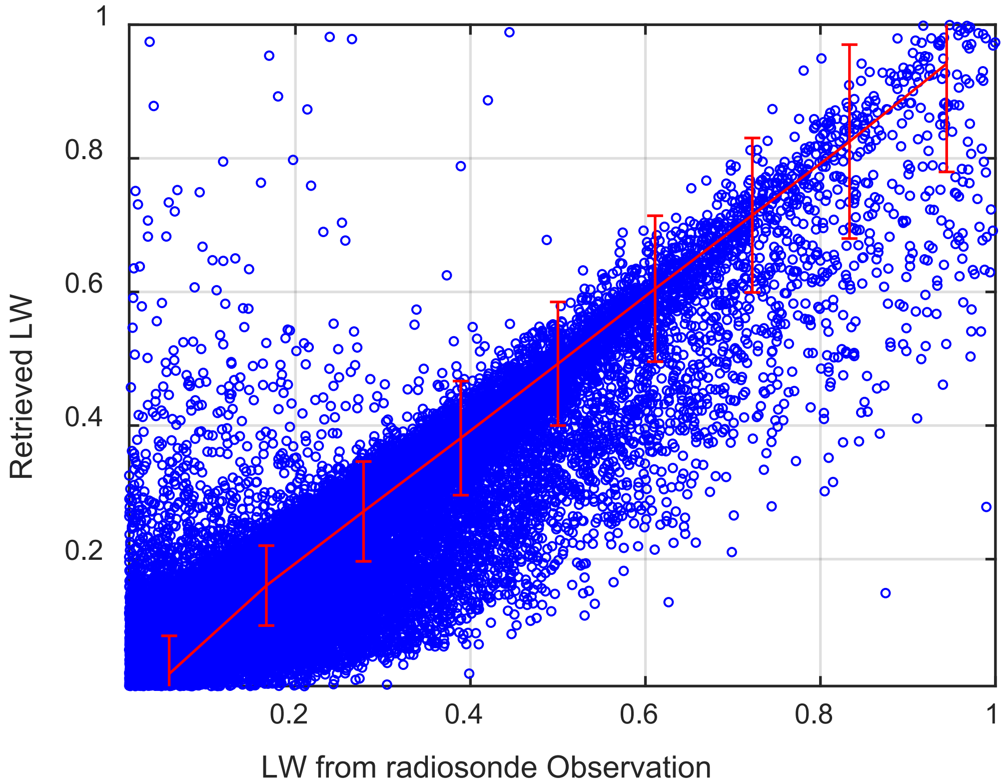

Figure 3. Comparison between retrieved liquid water and radiosonde observations (kg/m^2).

3.5 RadRainMask

3.5.1 Purpose

This function determines the rain flag at the radiometer measurements location from the radiometer brightness temperatures.

3.5.2 Input Data

Description	Source
Threshold on clould liquid burden to indicate rain	Static Auxiliary Data
Threshold on 18.7 GHz brightness temperature to indicate rain	Static Auxiliary Data
Equalized brightness temperatures at each AMR channel (18.7. 23.8, and 34.0 GHz).	RadEqualizeTb (L1B)
Land/sea mask flag	RadLandSeaMask (L2)
Sea ice flag	RadSeaIceMask (L2)
Integrated cloud liquid water content (cloud burden)	RadCloudLiqWater (L2)

3.5.3 Output Data

Description
Rain flag

3.5.4 Mathematical Statement

Rain is very absorptive in the microwave. Over the ocean, it will increase the brightness temperature observed by the AMR significantly and proportional to the rain rate. The cloud liquid water algorithm for the AMR will interpret rain as anomalously high cloud liquid water. A threshold can be placed on the retrieved cloud liquid water to indicate rain. A second test is to look for 18.7 GHz brightness temperature above some threshold. Over the ocean, only rain will cause the 18.7 GHz brightness temperature to rise above ~200 K.

The rain masking flag is computed using the following conditional expression:

$$f(TB_{18}, lsm, sim, L_Z) = \begin{cases} 1; & \begin{matrix} if\ TB_{18} > thres_{TB}, lsm = sea, sim = no\ seaice \\ if\ L_Z > thres_{clw}, lsm = sea, sim = no\ seaice \end{matrix} \\ 0; & otherwise \end{cases} \tag{3.5.1}$$

where, $TB_{18}$is the brightness temperature at 18.7 GHz channel, lsm is the land/sea masking flag information, sim is the sea-ice masking flag information, L_Z is the cloud liquid water content, and $thres_{TB}$ and $thres_{clw}$ are the associated thresholds for the 18.7 GHz equalized brightness temperature and cloud liquid content, respectively.

The recommended value for $thres_{clw}$ is 0.75 kg/m^2 and a recommended value for $thres_{TB}$ is 200 K. It should be noted that the rain flag will not be set if the sea ice flag is set or when the provided land/sea flag indicates land or coastal oceans.

3.5.5 Accuracy

This algorithm is shown to give reasonable distributions for rain. The first figure shows the climatological distribution of rain from the TRMM satellite. The second figure shows the average of the rain flag for 200 days of AMR data. The rain flag will never be set over land, coastal ocean, and over sea ice.

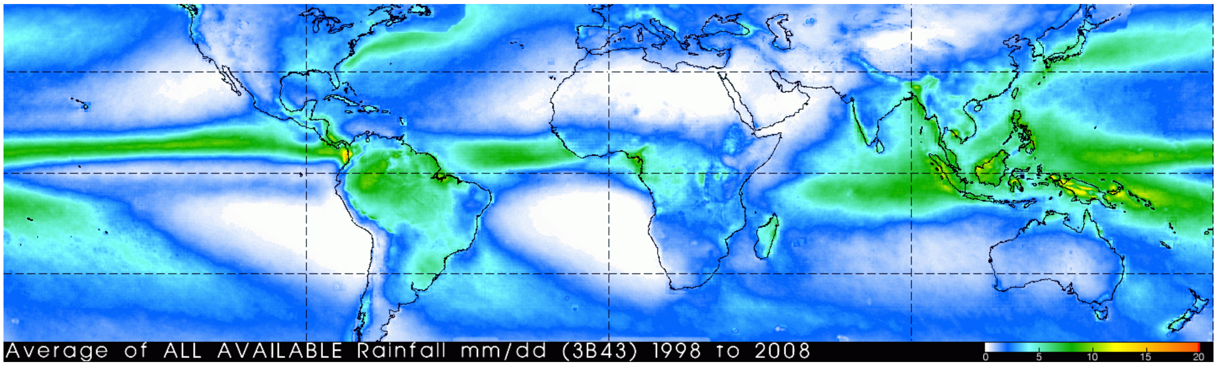

Figure 4. Rainfall climatology from TRMM.

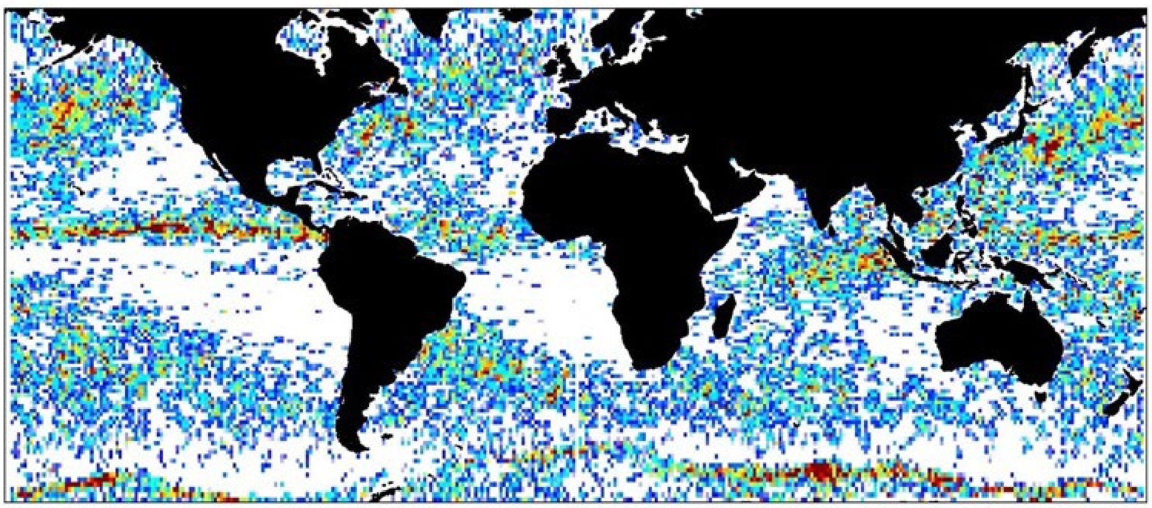

Figure 5. 200-day average of AMR rain flag.

3.6 RadWindSpeed

3.6.1 Purpose

This function computes sea surface wind speed from the radiometer brightness temperatures.

3.6.2 Input Data

Description	Source
Retrieval coefficients to compute the sea surface wind speed.	Static Auxiliary Data
Equalized brightness temperatures at each AMR channel (18.7. 23.8, and 34.0 GHz).	RadEqualizeTb (L1B)
Land/sea mask flag	RadLandSeaMask (L2)
Sea ice flag	RadSeaIceMask (L2)
Rain flag	RadRainMask (L2)

3.6.3 Output Data

Description
Sea surface wind speed
Quality flag for sea surface wind speed.

3.6.4 Mathematical Statement

This algorithm is based upon [4]. The wind speed, W, is computed using the following:

$$\mathrm{W} = w_0 + \sum_{i=1}^{3}[w_1(f_i) * T_b(f_i) + w_2(f_i) * [T_b(f_i)]^2 + w_3(f_i) * [T_b(f_i)]^3] \tag{3.6.1}$$

where $T_b(f_i)$ are the equalized AMR brightness temperatures for each frequency, f_i, with i = 1 to 3 corresponding to the 18.7 GHz, 23.8 GHz, and 34.0 GHz frequencies, respectively. The wind speed retrieval coefficients are $w_0, w_1(f_i), w_2(f_i)$, and $w_3(f_i)$.

These coefficients are derived from a multi-linear regression of modeled AMR brightness temperatures to near surface wind speed. The modeled brightness temperatures are computed using atmospheric profiles from island radiosonde observations and cloud liquid water profiles from a cloud model, combined with statistical distributions of surface wind speed and sea surface temperature.

The quality flag is set to bad when any one of the provided rain or sea ice flags are set, or when the provided land/sea flag indicates land or coastal oceans.

3.6.5 Accuracy

Comparison of sea surface wind speeds from radiosondes and from the algorithm using the brightness temperatures is shown in the scatter plot below. The sea surface wind speed that is compared to the algorithm is derived from the radiosonde temperature and humidity profile. The accuracy of the wind speeds from the radiometer brightness temperatures is 0.79 m/s.

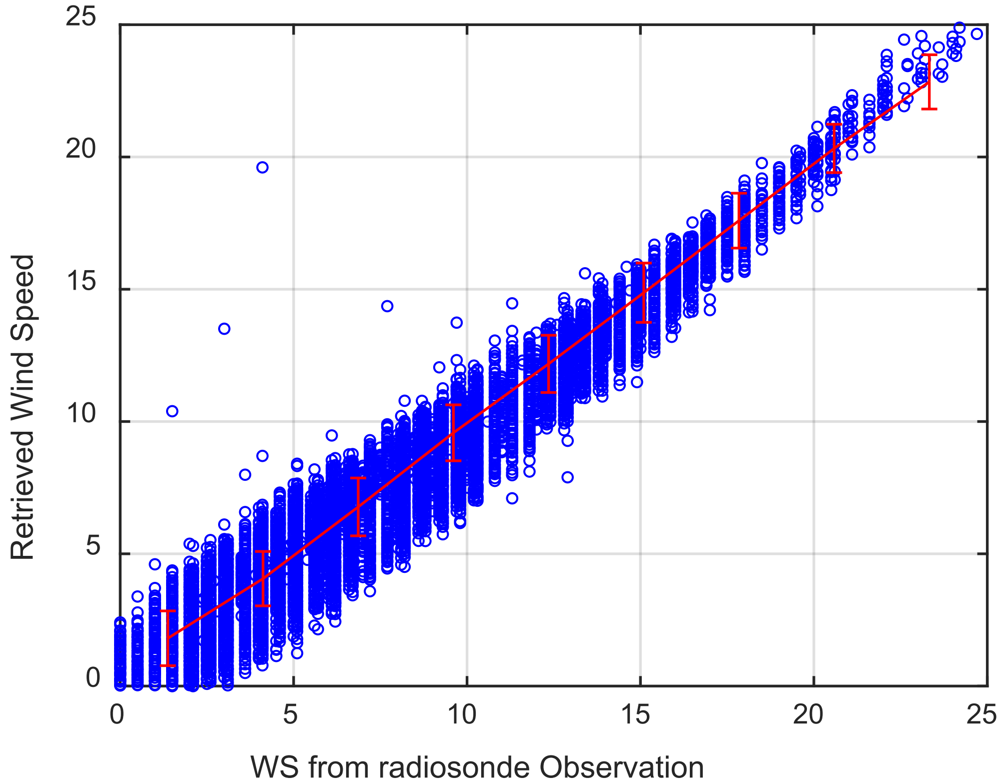

Figure 6. Comparison between retrieved wind speeds and radiosonde measurements (m/s).

3.7 RadPathDelaySea

3.7.1 Purpose

This function computes path delay in the sea region from the radiometer brightness temperatures.

3.7.2 Input Data

Description	Source
Retrieval coefficients to compute the wet troposphere path delay over open oceans.	Static Auxiliary Data
Equalized brightness temperatures at each AMR channel (18.7. 23.8, and 34.0 GHz).	RadEqualizeTb (L1B)
Integrated cloud liquid water content (cloud burden)	RadCloudLiqWater (L2)
Sea surface wind speed	RadWindSpeed (L2)
Land/sea mask flag	RadLandSeaMask (L2)
Sea ice flag	RadSeaIceMask (L2)
Rain flag	RadRainMask (L2)

3.7.3 Output Data

Description
Wet troposphere path delay in open ocean due to vapor only.
Wet troposphere path delay in open ocean due to vapor and liquid.
Quality flag for open ocean wet troposphere path delay.

3.7.4 Mathematical Statement

The formulation of the AMR wet troposphere algorithm and related geophysical parameters closely follows that of the TOPEX Microwave Radiometer [4].

First, an initial estimate of the vapor-induced path delay correction is made using the coefficients stratified by wind speed, but unstratified by path delay:

$$PD^{(g)} = B_0^{(g)} + \sum_{i=1}^{3} B^{(g)}(f_i) \ln\left[280 - T_b(f_i)\right] \qquad (3.7.1)$$

where $T_b(f_i)$ are the equalized AMR brightness temperatures (in Kelvin) for each frequency, f_i, with i = 1 to 3 corresponding to the 18.7 GHz, 23.8 GHz, and 34.0 GHz frequencies, respectively. $B_o^{(g)}$ and $B^{(g)}(f_i)$ are determined by linearly interpolating the path delay coefficients found in the static file bracketing the wind speed bins to the estimated wind speed. This initial path delay estimate is used only to choose the proper path delay coefficients from those that are stratified by path delay.

Next, path delay values are computed using the coefficients stratified by path delay. Two values are computed using the sets of coefficients which are valid for path delay values bracketing (drier and wetter) the estimate from previous equation (stratified by wind speed, but unstratified by path delay):

$$PD^{(1)} = B_0^{(1)} + \sum_{i=1}^{3} B^{(1)}(f_i) \ln\left[280 - T_b(f_i)\right] \qquad (3.7.2)$$

$$PD^{(2)} = B_0^{(2)} + \sum_{i=1}^{3} B^{(2)}(f_i) \ln\,[280 - T_b(f_i)] \tag{3.7.3}$$

where $B_0^{(1)}$, $B^{(1)}(f_i)$, $B_0^{(2)}$, and $B^{(2)}(f_i)$ are the retrieval coefficients. $B_0^{(1)}$and $B^{(1)}(f_i)$ are determined by linearly interpolating the path delay coefficients found in the drier path delay range row of the coefficient table to the wind speed estimate. $B_0^{(2)}$, and $B^{(2)}(f_i)$ are determined by linearly interpolating the path delay coefficients found in the wetter path delay range row of the coefficient table to the wind speed estimate.

These coefficients are derived from a regression of modeled AMR brightness temperatures to wet tropospheric path delay binned by surface wind speed and path delay value. The modeled brightness temperatures are computed using atmospheric profiles from island radiosonde observations and cloud liquid water profiles from a cloud model combined with statistical distributions of sea surface temperature. Separate model databases are generated for constant surface wind speeds of 0, 7, 14, 21 and 28 m/s.

The final estimate for the vapor-induced path delay component, $PD^{(f)}$ is obtained by linear interpolation between $PD^{(1)}$ and $PD^{(2)}$ to the initial path delay estimate. This linear interpolation assures that there will be no retrieval discontinuities across the stratification boundaries. The final total wet path delay is found by adding the small liquid component to the vapor-induced component:

$$PD_w = PD^{(f)} + D_L L_z \tag{3.7.4}$$

The quality flag is set to bad when any one of the provided rain or sea ice flags are set, or when the provided land/sea flag indicates land or coastal oceans.

3.7.5 Accuracy

The radiometer path delay retrieval algorithm is equivalent to the retrieval algorithm used on Jason-1, Jason-2, and Jason-3. The brightness temperature accuracy for the radiometer is expected to be no worse than the Jason-1 Microwave Radiometer brightness temperature accuracy. Comparisons with radiosondes indicate that the absolute accuracy of the Jason-1 Microwave Radiometer path delay retrieval is 0.74 cm [5]. Therefore, the path delay retrieval performance is expected to be <= 1.2 cm.

3.8 RadPathDelayNearLand

3.8.1 Purpose

This function computes path delay in the coastal, near-land region from the radiometer main beam brightness temperatures.

3.8.2 Input Data

Description	Source
Retrieval coefficients to compute the wet troposphere path delay near land.	Static Auxiliary Data
Main beam brightness temperatures at each AMR channel (18.7. 23.8, and 34.0 GHz).	RadMainBeamTb (L1B)
18.7 GHz main beam land fraction	RadLandSeaMask (L2)
Land/sea mask flag	RadLandSeaMask (L2)
Rain flag	RadRainMask (L2)

3.8.3 Output Data

Description
Wet troposphere path delay near land due to vapor only.
Wet troposphere path delay near land due to vapor and liquid. (Currently, liquid contribution is ignored, so this value is identical to value due to vapor only.)
Quality flag for near land wet troposphere path delay.

3.8.4 Mathematical Statement

This formulation of the near-land wet path delay retrieval is based upon [3]. First, an initial estimate of the vapor-induced path delay correction is made using the coefficients stratified by land fraction, but unstratified by path delay:

$$PD^{(g)} = B_0^{(g)} + \sum_{i=1}^{3} B^{(g)}(f_i) \ln\,[280 - T_b(f_i)] \tag{3.8.1}$$

where $T_b(f_i)$ are the main beam AMR brightness temperatures (in Kelvin) for each frequency, f_i, with i = 1 to 3 corresponding to the 18.7 GHz, 23.8 GHz, and 34.0 GHz frequencies, respectively. $B_o^{(g)}$ and $B^{(g)}(f_i)$ are determined by linearly interpolating the path delay coefficients found in the static file bracketing the land fraction bins to the 18.7 GHz main beam land fraction. This initial path delay estimate is used only to choose the proper path delay coefficients from those that are stratified by path delay.

Next, path delay values are computed using the coefficients stratified by path delay. Two values are computed using the sets of coefficients which are valid for path delay values bracketing (drier and wetter) the estimate from previous equation (stratified by land fraction, but unstratified by path delay):

$$PD^{(1)} = B_0^{(1)} + \sum_{i=1}^{3} B^{(1)}(f_i) \ln\,[280 - T_b(f_i)] \tag{3.8.2}$$

$$PD^{(2)} = B_0^{(2)} + \sum_{i=1}^{3} B^{(2)}(f_i) \ln\,[280 - T_b(f_i)] \tag{3.8.3}$$

where $B_0^{(1)}$, $B^{(1)}(f_i)$, $B_0^{(2)}$, and $B^{(2)}(f_i)$ are the retrieval coefficients.. $B_0^{(1)}$and $B^{(1)}(f_i)$ are determined by linearly interpolating the path delay coefficients found in the drier path delay range row of the coefficient table to the main beam land fraction. $B_0^{(2)}$, and $B^{(2)}(f_i)$ are determined by linearly interpolating the path delay coefficients found in the wetter path delay range row of the coefficient table to the main beam land fraction.

These coefficients are derived from a regression of modeled AMR brightness temperatures to wet tropospheric path delay binned by land fraction and path delay value. The modeled brightness temperatures are computed using atmospheric profiles from island radiosonde observations and cloud liquid water profiles from a cloud model combined with statistical distributions of sea surface temperature and land surface brightness.

The final estimate for the vapor-induced path delay component, $PD^{(f)}$, is obtained by linear interpolation between $PD^{(1)}$ and $PD^{(2)}$ to the initial path delay estimate. This linear interpolation assures that there will be no retrieval discontinuities across the stratification boundaries.

The quality flag is set to bad when the provided land/sea flag indicates land or open ocean, and good when this flag is set to near land.

3.8.5 Accuracy

This algorithm has been shown to produce retrieval errors of less than 1.5 cm RMS in the coastal region from 0 – 75 km from the coast. The error decreases sharply as the distance from land increases.

The algorithm error when applied to the AMR is estimated to be less than 0.8 cm up to 15 km from land, less than 1.0 cm within 10 km from land, less than 1.2 cm within 5 km from land and less than 1.5 cm up to the coastline. This is estimated from detailed simulations and validated by comparisons with measured AMR data. While the quality flag is set to good near land, the computed path delays are susceptible to rain contamination.

3.9 RadPathDelayGlobal

3.9.1 Purpose

This function combines the path delay estimates in the sea and near-land regions to produce a global path delay estimate.

3.9.2 Input Data

Description	Source
Land fraction linear interpolation boundary between coastal and open ocean wet troposphere path delay.	Static Auxiliary Data
Wet troposphere path delay in open ocean due to vapor only.	RadPathDelaySea (L2)
Wet troposphere path delay in open ocean due to vapor and liquid.	RadPathDelaySea (L2)
Quality flag for open ocean wet troposphere path delay.	RadPathDelaySea (L2)
Wet troposphere path delay near land due to vapor only.	RadPathDelayNearLand (L2)
Wet troposphere path delay near land due to vapor and liquid.	RadPathDelayNearLand (L2)
Quality flag for near land wet troposphere path delay.	RadPathDelayNearLand (L2)
18.7 GHz main beam land fraction	RadLandSeaMask (L2)
Land/sea mask flag	RadLandSeaMask (L2)
Sea ice flag	RadSeaIceMask (L2)
Rain flag	RadRainMask (L2)

3.9.3 Output Data

Description
Wet troposphere path delay (positive value) globally due to vapor only.
Wet troposphere correction (negative value to be added to range) globally due to vapor and liquid.
Quality flag for global wet troposphere correction.

3.9.4 Mathematical Statement

This function is provided with path delays that are separately computed over the open ocean and near land regions. This algorithm then combines the two estimates based on land-sea masking flags and linear interpolation based upon the main beam land fraction for the 18 GHz channel, LF_{18}, and a land fraction linear interpolation boundary, LFI.

When the land/sea flag is set to open ocean the wet troposphere correction is defined to be the value computed from the open ocean retrieval algorithm in RadPathDelaySea.

When the land/sea flag is set to "coasts" (i.e., value of 1), the value is set to the value computed by the near land retrieval algorithm in RadPathDelayNearLand when $LF_{18} > LFI$.

To avoid the discontinuity at the open ocean/near land boundary, in the regions where $LF_{18} < LFI$ a linear interpolation of the open ocean and near land values are used, e.g., $(LF_{18}/LFI) * near\_land\_value + (1 - LF_{18}/LFI) * open\_land\_value$.

As a final step, the wet troposphere correction to range (applied by adding to range) is computed by multiplying the wet troposphere path delay due to vapor and liquid by -1.

The quality flag is set to bad when any one of the provided rain or sea ice flags are set, or when the provided land/sea flag indicates land.

3.9.5 Accuracy

Refer to open ocean and near land path delay retrieval accuracies (Sections 3.7.5 and 3.8.5 for path delay retrieval accuracy in open ocean and near land.

3.10 RadWaterVapor

3.10.1 Purpose

This function computes water vapor content (integrated) from the path delay due to vapor estimates.

3.10.2 Input Data

Description	Source
Retrieval coefficients to compute the integrated water vapor content.	Static Auxiliary Data
Wet troposphere path delay (positive value) globally due to vapor only.	RadPathDelayGlobal (L2)
Quality flag for global wet troposphere correction.	RadPathDelayGlobal (L2)
Land/sea mask flag	RadLandSeaMask (L2)
Sea ice flag	RadSeaIceMask (L2)
Rain flag	RadRainMask (L2)

3.10.3 Output Data

Description
Integrated water vapor content.
Quality flag for integrated water vapor content.

3.10.4 Mathematical Statement

This algorithm is based upon [4]. The integrated water vapor content, V_Z is computed from path delay due to vapor estimates using:

$$V_z = \frac{PD^{(f)}}{V_0 + V_1 * PD^{(f)} + V_2 * PD^{(f)} * PD^{(f)}} \tag{3.10.1}$$

where V_0, V_1, and V_2 are the integrated vapor retrieval coefficients.

The quality flag is set to bad when any one of the provided rain or sea ice flags are set, or when the land/sea flag indicates land or coastal oceans, or when the quality flag for the global wet troposphere path delay due to vapor is bad.

3.10.5 Accuracy

Monte Carlo Simulation of the algorithm using the absolute accuracy of the Jason 1 Microwave Radiometer path delays (0.74 cm) and equation 3.10.1 indicates that the accuracy of water vapor content is 0.27 g/cm^2.

3.11 RadAttSigma0

3.11.1 Purpose

This function computes the two-way atmospheric attenuation in sigma0 at the three relevant frequencies for SWOT, namely Ku and C band for the nadir altimeter and Ka band for KaRIn.

3.11.2 Input Data

Description	Source
Retrieval coefficients to compute the two-way atmospheric attenuation in sigma0 at each of the radar frequencies from brightness temperatures, including the number of radar frequencies and the frequency ID for each of those sets of coefficients.	Static Auxiliary Data
Equalized brightness temperatures at each AMR channel (18.7. 23.8, and 34.0 GHz).	RadEqualizeTb (L1B)
Land/sea mask flag	RadLandSeaMask (L2)
Sea ice flag	RadSeaIceMask (L2)

3.11.3 Output Data

Description
Two-way atmospheric attenuation in sigma0 at each of the radar frequencies.
Quality flag for the sigma0 atmospheric attenuation.

3.11.4 Mathematical Statement

The Sigma0 atmospheric 2-way attenuation at the altimeter frequency ω, $\tau(\omega)$, is obtained from a linear combination of the AMR brightness temperatures using the following relation:

$$\tau(\omega) = 2 \cdot \{c_0(\omega) + \sum_{i=1}^{3} c_i(\omega) ln[290 - T_b(f_i)] + c_{i+3}(\omega) ln[290 - T_b(f_i)]^2\} \quad (3.11.1)$$

where $T_b(f_i)$ are the equalized brightness temperatures (in Kelvin) for each frequency, f_i, with i = 1 to 3 corresponding to the 18.7 GHz, 23.8 GHz, and 34.0 GHz frequencies, respectively. The coefficients $c_i(\omega)$ are stratified by the radiometer 18.7 GHz brightness temperature, and are dependent on altimeter frequency. There is one set of coefficients for $T_b(18.7GHz)$ less than 180 K, one set for $T_b(18.7GHz)$ greater than 180K but less than 250K and one set for $T_b(18.7GHz)$ greater than 250K.

The algorithm coefficients were derived using a large database of modeled brightness temperatures. The brightness temperatures were derived using a radiative transfer model along with globally distributed open ocean radiosonde observations. The radiative transfer model is described in [5]. These modeled TBs are for non-precipitating conditions. To add the contribution from rain to these modeled TBs, a simple parameterized algorithm for rain attenuation is used. The extinction coefficient from precipitation as a function of rain rate, RR, and frequency is from [6]:

$$k_{ext\_rain} = k_1 RR^b / 4.34 \qquad \text{(Np/km)} \qquad (3.11.2)$$

where

$$k_1 = 4.21e - 5 * f^{2.42} \qquad (3.11.3)$$

$$b = \begin{cases} 0.851 * f^{0.158} & f < 8.5GHz \\ 1.41 * f^{-0.0779} & 8.5 \leq f < 25GHz \\ 2.63 * f^{-0.272} & f \geq 25GHz \end{cases} \tag{3.11.4}$$

The path integrated attenuation from precipitation is the product of the extinction coefficient and the rain column height. An approximation for rain column height as a function of surface temperature from [7] is used:

$$H_{rain} = \begin{cases} 1 + 0.14 * \left(T_{sfc} - 273\right) - 0.0025 * \left(T_{sfc} - 273\right)^2, T_{sfc} \leq 301K \\ 2.96, T_{sfc} > 301K \end{cases} \tag{3.11.5}$$

and then

$$\tau_{rain} = k_{ext\_rain} H_{rain} \qquad \text{(Np)} \tag{3.11.6}$$

The path integrated attenuation from the precipitation is added to the non-precipitating path integrated attenuation from the radiosonde database, the brightness temperatures are re-computed using the 1-layer atmospheric radiative transfer model described in [8].

The quality flag is set to bad when the provided sea ice flag is set, or when the land/sea flag indicates land or coastal oceans.

When the AMR brightness temperatures are contaminated by land, the Sigma0 atmospheric 2-way attenuation at the altimeter frequency ω, $\tau(\omega)$, is obtained from the global path delays.

$$\tau(\omega) = 2 * (k_0(\omega) - k_1(\omega) * PD) \tag{3.11.7}$$

where $k_i(\omega)$ are the retrieval coefficients, and PD is the global path delay (negative quantity).

When there is no land contamination, the quality flag is set to good if the sea ice flag is set to “no sea ice”. and the quality flags for all three brightness temperatures are good. When there is land contamination, the quality flag is set to good if the sea ice flag is set to “no sea ice”, the path delay quality flag is good, and the land/sea mask flag is set to “near land”.

3.11.5 Accuracy

The residual errors of the retrieval algorithm as a function of attenuation for Ku and C-band are shown in the figure below. The residual 2-way attenuation algorithm error is 0.03dB at Ku-band and 0.004dB at C-band for clear air to moderate precipitating conditions. For heavy precipitation, the 2-way algorithm error is 0.2dB at Ku-band and 0.02dB at C-band. These errors describe the residual algorithm error and do not represent the absolute accuracy of the derived attenuation. The absolute accuracy will depend on a number of factors, including the absolute accuracy of the AMR TBs and the accuracy of the models used to derive the TB database. The absolute accuracy has not been assessed for this algorithm, but can be assessed from on-orbit data. The absolute accuracy is expected to be good for clear air and light precipitation and degrade for larger values of attenuation. As shown in Figure 8 the accuracy of the 2-way atmospheric attenuation at Ka band is less than 0.1 dB at 2-way attenuations less than 1dB and grows rapidly to 0.6 dB at 2-way attenuations of 20 dB. Figure 9 shows a comparison of the Ka-band algorithm applied to Jason-3 cycle 10 to the Ka-band attenuation derived from the SARAL Ka-band altimeter (adapted from [9]). The global distribution and magnitude of attenuation agree qualitatively between the algorithm applied to Jason-3 and SARAL.

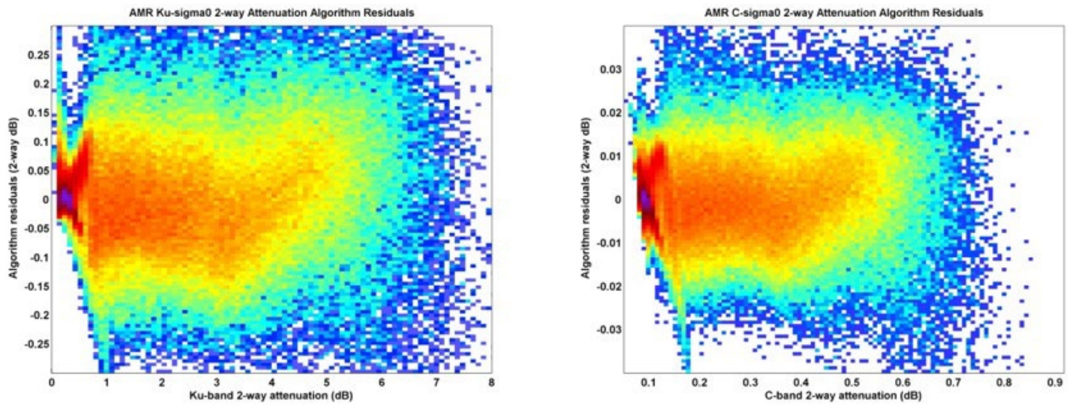

Figure 7. Sigma0 attenuation algorithm residuals for Ku (upper left) and C (upper right) bands., as a function of attenuation.

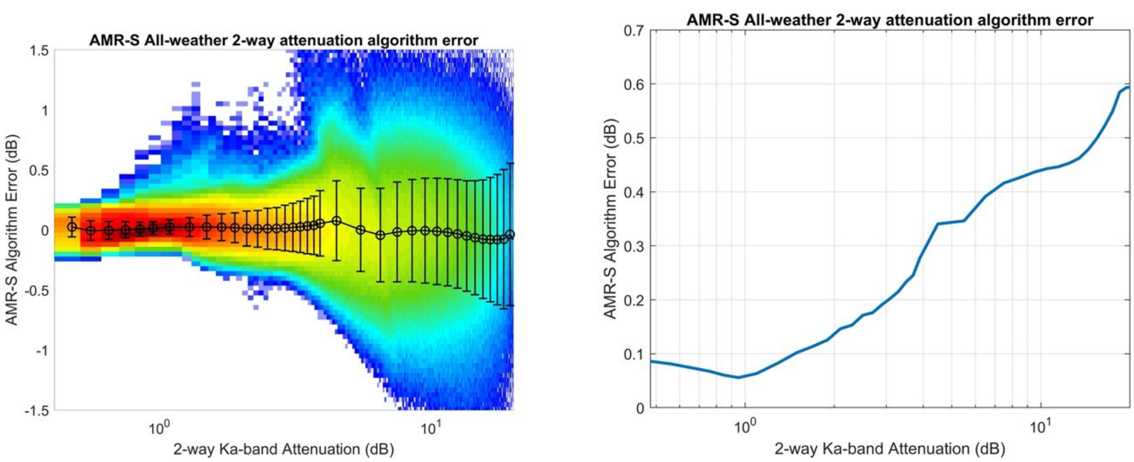

Figure 8. Sigma0 attenuation algorithm residuals for Ka (35.75 GHz) as a function of attenuation.

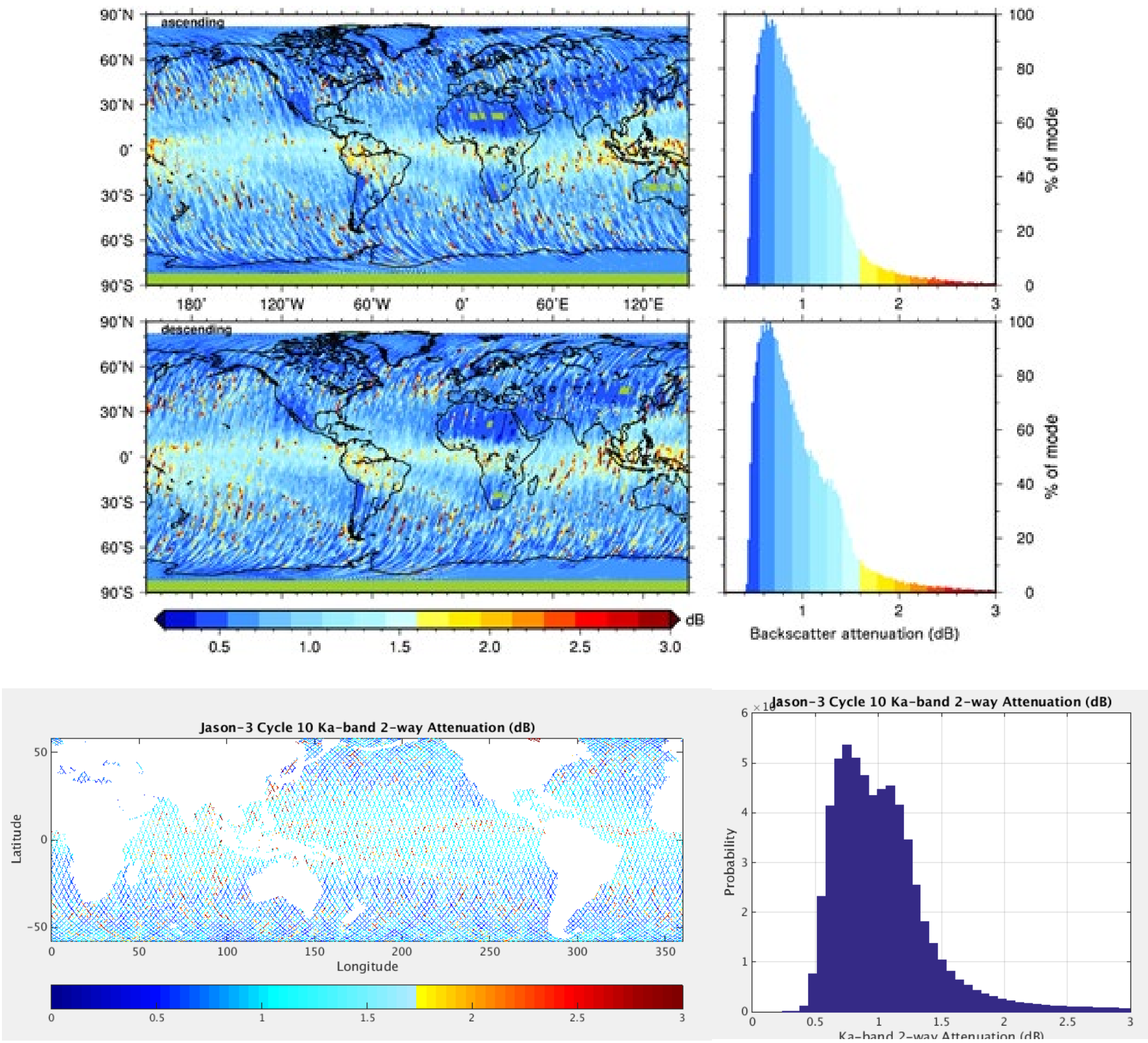

Figure 9. Ka-band attenuation derived from SARAL [9] (top) and after applying attenuation algorithm to Jason-3 cycle 10 (bottom). Note, the difference in the histograms is due in part to the different global sampling of the comparison; SARAL has samples over land and in polar regions resulting in higher peak around low attenuation values.

4 References

[1] "SWOT Science Requirements Document, JPL D-61923," Jet Propulsion Laboratory, 2018.

[2] C. Chae and N. Picot, "SWOT Level 2 Radiometer Geophysical Data Record Product," D-56417, Jet Propulsion Laboratory, Pasadena, 2022.

[3] S. Brown, "A novel near-land radiometer wet path-delay retrieval algorithm: Application to the Jason-2/OSTM Advanced Microwave Radiometer," *IEEE Trans. Geosci. Remote Sens.,* vol. 48(4), pp. 1986-1992, 2010.

[4] S. J. Keihm, M. A. Janssen and C. S. Ruf, "TOPEX/POSEIDON microwave radiometer (TMR): III. Wet troposphere range correction algorithm and pre-launch error budget," *IEEE Trans. Geosci. Remote Sensing,* vol. 33, pp. 147-161, Jan. 1995.

[5] S. Brown, C. Ruf, S. Keihm and A. Kitiyakara, "Jason microwave radiometer performance and on-orbit calibration.," *Marine Geodesy,* vol. 27 (1), pp. 199-220, Jan.-June 2004.

[6] R. Ulaby, R. Moore and A. Fung, Microwave Remote Sensing: Active and Passive, vol. III, Artech House, Inc., pp. 1310-1312.

[7] F. J. Wentz and R. W. Spencer, "SSM/I Rain Retrievals within a Unified All-Weather Ocean Algorithm," *J. of Atmos. Sci.,* vol. 55, pp. 1613-1627, 1998.

[8] S. Brown, C. Ruf and D. R. Lyzenga, "An emissivity based wind vector retrieval algorithm for the WindSat polarimetric radiometer," *IEEE Trans. Geosci. Remote Sens.,* vol. 44(3), pp. 611-621, 2006.

[9] J. Lillibridge, R. Scharoo, S. Abdalla and D. Vandemark, "One- and two-dimensional wind speed models for Ka-band altimetry," *J. Atmos. Oceanic Technol.,* vol. 31, pp. 630-638, 2014.

Appendix A. **Acronyms**

AMR	Advanced Microwave Radiometer
ATBD	Algorithm Theoretical Basis Document
CNES	Centre National d'Études Spatiales
JPL	Jet Propulsion Laboratory
NASA	National Aeronautics and Space Administration
SWOT	Surface Water Ocean Topography
TBC	To Be Confirmed
TBD	To Be Determined

